Matter

Article

Meta-structured electret heterointerface for resilient and adaptive tele-perception in embodied intelligence

Graphical abstract

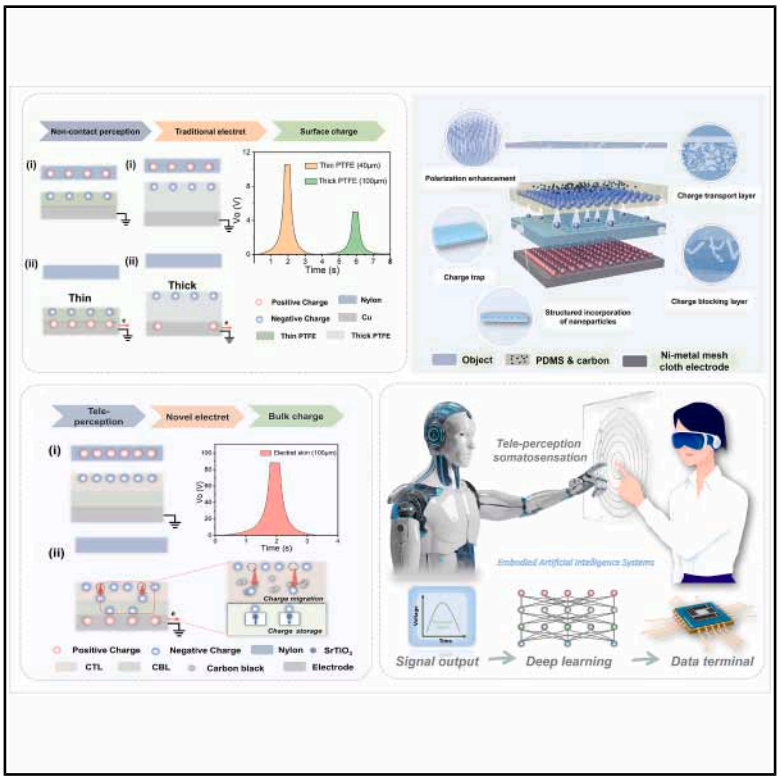

Highlights

- NAES uses a dual-layer heterointerface for 3-m range and high electrostatic sensitivity
- Maintains robust electrostatic detection under conditions where conventional sensors fail
- Embedded deep learning filters noise and resolves signal ambiguity in real time
- Delivers 98.32% accuracy with fast, adaptive perception in cluttered environments

Authors

Yan Du, Penghui Shen, Houfang Liu, ..., Tianling Ren, Zhong Lin Wang, Di Wei

Correspondence

dpc31@cam.ac.uk (D.C.), rentl@tsinghua.edu.cn (T.R.), zlwang@binn.cas.cn (Z.L.W.), dw344@cam.ac.uk (D.W.)

In brief

A nano-architectured electret skin, incorporating a charge transport layer for dynamic redistribution and a charge blocking layer for electrostatic confinement, shifts from conventional surface-confined charge to bulk charge retention, thereby facilitating meter-scale, high-sensitivity tele-perception with algorithm-assisted decoupling of environmental interferences and establishing a next-generation sensory paradigm for embodied intelligence beyond the spatial and functional constraints of contact-based systems.

Du et al., 2025, Matter 8, 102363
December 3, 2025 © 2025 Elsevier Inc. All rights are reserved, including those for text and data mining, AI training, and similar technologies.
https://doi.org/10.1016/j.matt.2025.102363

CellPress

Matter

CellPress

Article

Meta-structured electret heterointerface for resilient and adaptive tele-perception in embodied intelligence

Yan Du,[1,2] Penghui Shen,[3,6] Houfang Liu,[3] Zhiwei Zhang,[1] Feiyao Yang,[1] Daping Chu,[5,*] Tianling Ren,[3,*] Zhong Lin Wang,[1,4,*] and Di Wei[1,5,7,*]

[1]Beijing Institute of Nanoenergy and Nanosystems, Chinese Academy of Sciences, Beijing 101400, China
[2]School of Nanoscience and Engineering, University of Chinese Academy of Sciences, Beijing 100049, China
[3]School of Integrated Circuits & Beijing National Research Center for Information Science and Technology, Tsinghua University, Beijing 10084, China
[4]Beijing Key Laboratory of Micro-Nano Energy and Sensor, Center for High-Entropy Energy and Systems, Beijing Institute of Nanoenergy and Nanosystems, Chinese Academy of Sciences, Beijing 101400, P.R. China
[5]Centre for Photonic Devices and Sensors, University of Cambridge, 9 JJ Thomson Avenue, CB3 0FA Cambridge, UK
[6]These authors contributed equally
[7]Lead contact
*Correspondence: dpc31@cam.ac.uk (D.C.), rentl@tsinghua.edu.cn (T.R.), zlwang@binn.cas.cn (Z.L.W.), dw344@cam.ac.uk (D.W.)
https://doi.org/10.1016/j.matt.2025.102363

PROGRESS AND POTENTIAL Tele-perception technologies were essential for advancing embodied artificial intelligence, yet conventional electret-based systems suffered from rapid charge dissipation and environmental instability, limiting their real-world applicability. Here, we presented a nano-architectured electret skin (NAES) with a meta-structured heterointerface to overcome these challenges. The NAES transitioned from surface-confined charge to bulk charge retention using a dual-layer structure that enabled a record 3-m sensing range with high sensitivity. Integrated deep learning resolved environmental noise in real time, achieving 98.32% identification accuracy in cluttered settings. Beyond robotics, the NAES established a universal charge-trapping framework for neuromorphic computing and fault-tolerant Internet of Things (IoT) systems, addressing cross-disciplinary challenges in energy-efficient sensing. By bridging electrostatic engineering with machine intelligence, this work opened avenues for autonomous systems operating in dynamic environments.

SUMMARY

Tele-perception is essential for embodied artificial intelligence, enabling adaptive systems and real-time human-machine interactions (HMIs). However, conventional electret-based systems suffer rapid charge dissipation, limiting the range to under 1 m and reducing stability in dynamic environments. Here, we propose a meta-structured heterointerface with a nano-architectured electret skin (NAES). It integrates a charge transport layer (CTL) for dynamic redistribution and a charge blocking layer (CBL) for electrostatic trapping, enabling bulk charge retention instead of surface-confined charge. This architecture achieves a 3-m sensing range with high sensitivity, $\Delta V/\Delta d = 21.8$, significantly outperforming traditional systems. Signal processing algorithms decouple electrostatic responses from humidity and Gaussian noise, ensuring robust, adaptive perception. The system replaces the conventional "approach→touch→interact" sequence with a closed-loop "tele-perception→interact" model. This work establishes a universal charge-trapping paradigm with broad implications for remote control, neuromorphic computing, and real-world applications of embodied intelligence systems.

INTRODUCTION

Embodied intelligence[1,2] theory asserts that object perception is intrinsically shaped by the ability to engage in physical interactions.[3–5] Tele-perception is critical for embodied intelligence, driving the evolution of autonomous systems[6,7] and human-machine interactions (HMIs)[8–10] with unparalleled adaptability. By orchestrating active environmental cognition through

All rights are reserved, including those for text and data mining, AI training, and similar technologies.

spatiotemporal charge field coupling, it transcends passive sensing[11,12] paradigms, empowering machines with real-time adaptive interaction and autonomous behavioral plasticity in dynamically evolving scenarios. While foundational, conventional tele-perception sensors rely on diverse physical principles tailored to specific applications, each faces distinct challenges. Infrared sensors,[13,14] which are used for security and fire monitoring,[15,16] are hindered by humidity-induced signal attenuation. Ultrasonic sensors,[17,18] which are employed for navigation, struggle in cluttered environments due to acoustic scattering.[19] Laser sensors,[20–22] offering submillimeter precision in industrial automation,[23] degrade in the presence of airborne particulates. Capacitive sensors,[24–26] which are used for proximity sensing, suffer from instability under temperature and humidity fluctuations. Magnetic sensors,[27–29] crucial in transport systems,[30,31] are compromised by electromagnetic interference. Optical sensors,[32] relying on light modulation[33,34] for metrology and imaging, require an unobstructed line of sight and fail under low illumination or reflective surfaces. These modalities are collectively constrained by environmental fragility, limited operational ranges, and modality-specific blind spots, significantly impairing their performance in interference-prone, dynamic environments. Such intrinsic limitations, spanning environmental adaptability, range constraints, and susceptibility to interference, underscore the critical need for transformative sensing paradigms.

Emerging electroreceptor-based[35] tele-perception overcomes these limitations through charge-trapping architectures and adaptive signal processing. In our previous work, the concept of tele-perception[36] was introduced through the integration of inorganic nanoparticle arrays to create stable charge traps, inspired by the electrosensory system of the platypus. This innovation amplifies local electric fields and sustains charge retention, enabling remote detection of human presence at record-high ranges (1.55 m), with a sensitivity metric ($\Delta V/\Delta d$ = 14.2) surpassing conventional benchmarks. Unlike modality-specific traditional sensors, this system integrates multimodal data fusion (proximity,[37] motion,[38] and environmental fluctuations[39]) with machine learning algorithms[40,41] to dynamically filter noise and resolve signal ambiguities in real time. Importantly, its reliance on electric field perturbations eliminates line-of-sight dependencies and mitigates interference from humidity, particulates, or electromagnetic clutter. This paradigm shift[42] not only circumvents the physical and environmental limitations of legacy systems but also establishes a scalable framework for high-resolution, context-aware sensing in complex, dynamic environments, laying the foundation for next-generation autonomous systems and enhanced human-environment interactions. Despite advances in bioinspired tele-perception, conventional electret materials in electroreceptor-based systems remained constrained by surface-confined charge. Environmental humidity and airborne ions accelerate charge dissipation, while interfacial electric fields between surface charges and electrodes induce leakage, undermining stability. These challenges mirror critical bottlenecks in remote sensing technologies, all constrained by charge instability, exposing a universal issue for electrostatic-controlled systems. Overcoming this requires a shift from surface-confined to bulk charge stabilization. Achieving this would address resilience and adaptability limitations in tele-perception, enabling transformative applications, such as autonomous robots navigating unstructured environments and fault-tolerant Internet of Things (IoT) networks operating in dynamic conditions, where robust environmental interaction is essential.

Herein, a meta-structured heterointerface with a nano-architectured electret skin (NAES) is proposed, which redefines charge transport design and fundamentally overcomes the limitations of conventional electret materials by achieving the first transition from surface-confined charge retention to bulk charge trapping. The charge transport layer (CTL), composed of carbon-black-doped PDMS, introduces nanoscale charge capture sites that enable dynamic charge redistribution, ensuring rapid electron mobility for real-time environmental responsiveness. Complementarily, the charge blocking layer (CBL), embedded with ferroelectric $SrTiO_3$ nanoparticles, leverages polarization-induced bulk charge trapping to stabilize electrostatic retention against thermal and humidity variations. This meta-structuring decouples electrostatic signal modulation from environmental noise, a capability unattainable in homogeneous electrets or conventional sensors. The NAES achieves a 3-m sensing range with $\Delta V/\Delta d$ = 21.8, surpassing existing tele-perception technologies by orders of magnitude. Crucially, its reliance on electric field perturbations, rather than photons, sound waves, or capacitive coupling, eliminates modality-specific blind spots such as optical obstructions or acoustic scattering, enabling non-line-of-sight perception in cluttered environments. The advanced electroreceptor-based tele-perception capabilities of the NAES enable resilient HMIs, successfully demonstrating control of robot movement and unmanned aerial vehicles (UAVs) in high-darkness and high-humidity conditions. To further enhance its capabilities, integrated deep learning algorithms are employed to translate 2D electrostatic data into multidimensional information. By training on noise-inclusive datasets, the algorithm dynamically filters Gaussian noise and resolves signal ambiguities in real time, achieving adaptive perception without compromising system latency and an impressive 98.32% identification accuracy in cluttered environments. This represents a shift from the traditional "approach→touch→interact" paradigm to a closed-loop "tele-perception→interact" dynamic interaction framework. This breakthrough ushers in a new era of pervasive sensing and embodied artificial intelligence systems, enabling transformative applications in robotics and HMIs and paving the way for future advancements in robust tele-perception technologies for autonomous and adaptive systems.

RESULTS

Design of the NAES for tele-perception systems

Non-contact sensing emerged as a critical technology for environmental monitoring and HMI, enabling remote detection of external stimuli without physical interaction. However, conventional electret-based sensors were fundamentally constrained by surface-confined electrostatic charge accumulation, a challenge exacerbated by increased material thickness, which disrupted charge equilibrium and diminished operational efficiency (Figure 1A). Environmental perturbations such as airborne particulates and humidity variations further accelerated charge

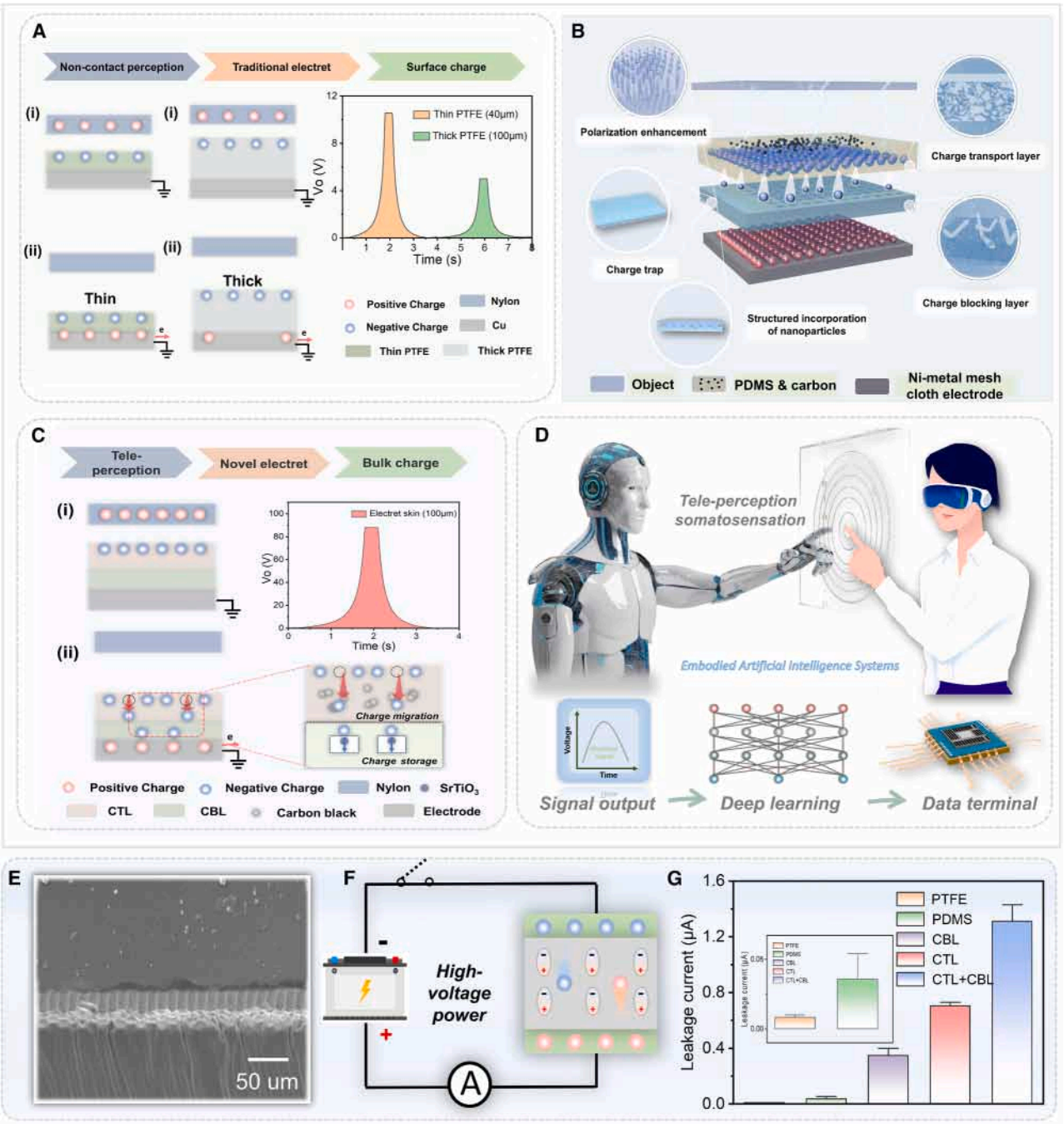

Figure 1. Schematic of the NAES system for high-performance tele-perception

(A) Working principle of traditional non-contact sensors based on electret materials.
(B) Three-dimensional structural schematic of the NAES.
(C) Working principle of the NAES.
(D) Schematic of the tele-perception based on the NAES system and deep learning algorithms.
(E) Cross-sectional SEM image of the NAES.
(F) Structural diagram of the leakage current test.
(G) Comparison of leakage current tests in different electret materials.

dissipation, severely limiting long-term operational stability and practical sensing distances. These unresolved limitations underscore the urgent need for electret material engineering strategies that can decouple electrostatic signal retention from surface confinement while ensuring environmental resilience, which is a critical prerequisite for next-generation tele-perception systems. The operational principle of conventional electronic receptors relied on three sequential stages: surface charge generation, dielectric-layer charge migration, and electrode charge induction (Figure S1). While theoretically robust, this framework suffered from inherent inefficiencies. Excessive surface charge density created electrostatic repulsion that impeded migration, while environmental contaminants such as moisture and dust formed parasitic discharge pathways, collectively destabilizing the charge induction process. Such cascading failures highlighted the inadequacy of existing charge management paradigms in reconciling high sensitivity with environmental robustness.

To overcome these challenges, we designed a meta-structured heterointerface through an NAES, integrating three functionally synergistic components: a CTL, a CBL, and a Ni-metal mesh electrode (Figure 1B). The CTL, fabricated from carbon-black-doped polydimethylsiloxane (PDMS), utilized the high electrical conductivity of carbon black to establish nanoscale charge capture sites, significantly enhancing charge capture efficiency. This material selection balanced scalable synthesis and cost effectiveness while optimizing charge transport. However, interfacial charge leakage arose from electric field interactions between surface charges and induced charges at the bottom electrode, resulting in diminished charge density and sensor efficiency. To address this, we engineered a CBL via photolithographic patterning of microstructured PDMS embedded with ferroelectric $SrTiO_3$ nanoparticles. These nanoparticles generated spontaneous polarization fields that created deep charge traps, effectively suppressing recombination and minimizing charge loss. This design elevated both charge retention capacity and sensing fidelity. Complementing these layers, the Ni-metal mesh cloth served as a breathable, flexible electrode, combining mechanical robustness with environmental stability across diverse operational conditions. Its open grid architecture ensured minimal interference with electrostatic signal transmission while maintaining structural integrity under mechanical stress, which is a critical feature for wearable and adaptive systems (Figure S2).

The CTL, deposited onto the CBL via plasma treatment, facilitated a critical transition from surface-confined to bulk charge trapping through its heterointerface design, as demonstrated in Figure 1C. Integrated deep learning algorithms within the NAES architecture enhanced signal processing and pattern identification, improving noise suppression and operational adaptability (Figure 1D). Scanning electron microscopy (SEM) cross-section imaging revealed the NAES's well-defined multilayer structure with sharp CTL-CBL interfaces (Figure 1E). Leakage current measurements demonstrated the system's bulk charge retention capability (Figures 1F and 1G): the traditional electret material (PTFE) exhibited low leakage current, indicative of surface-confined charge, whereas the NAES's dual-layer architecture showed higher leakage current, suggesting effective bulk charge retention within the dielectric material. The upper CTL provided additional charge migration channels, while ferroelectric $SrTiO_3$ nanoparticles within the CBL generated a spontaneous polarization field that stabilized bulk charge trapping. This synergistic coupling between charge mobility and retention, mediated by the meta-structured heterointerface, resolved the inherent trade-off in conventional electrets between dynamic responsiveness and environmental stability. By decoupling charge migration (CTL) from trapping (CBL), the NAES achieved optimized charge equilibrium, enabling tele-perception capabilities with minimal signal degradation under humidity or thermal fluctuations.

Mechanisms of the NAES

The NAES architecture leveraged a dual charge management strategy, static polarization and dynamic charge redistribution, to harmonize electrostatic capture and retention. Within this framework, the CTL employed conductive carbon black dopants to establish spatially distributed charge capture sites, dynamically capturing approaching electrostatic charges through enhanced electron mobility. Concurrently, the CBL confined these charges within a spontaneous polarization field that stabilized bulk charge trapping, ensuring long-term retention and environmental resilience. To elucidate these mechanisms, we analyzed charge migration in PDMS with and without carbon black doping (Figure 2A, left). Undoped PDMS exhibited rapid surface charge dissipation dominated by electrode migration and ambient ion interactions. In contrast, carbon black doping introduced conductive percolation networks that intercepted migrating charges, redirecting them toward charge capture sites. Figure 2A (right) illustrates a schematic of the theoretical conceptual model for the chronological mechanism of PDMS with and without carbon black doping. The transition time from capacitive effects to charge diffusion/migration effects was defined as t_i. Initially, capacitive effects governed charge induction, accumulating charges on electrodes until saturation. Post-saturation, charge migration through carbon networks dominated, with carbon particles acting as metastable capture sites that enhanced bulk charge. Notably, dielectric surface defects generated excess negative charges during contact-separation cycles, amplifying electrode induction efficiency. This dual-phase mechanism, capacitive induction followed by migration-driven trapping, synergistically elevated charge retention while circumventing saturation-induced performance limits. While the CTL effectively captured electrostatic charges, it exhibited insufficient control over charge migration pathways and kinetics. Rapid electron migration toward conductive electrodes induced charge leakage, degrading overall system performance. To mitigate this limitation, we introduced the CBL, which functioned as a physicochemical barrier between the dielectric layer and electrodes, modulating charge migration dynamics. The CBL decelerated charge migration rates, suppressing premature leakage to electrodes. To implement this design, a structured PDMS template was fabricated via photolithography, followed by high-speed spin coating of ferroelectric $SrTiO_3$ nanoparticles onto the elastomer surface. Comparative analysis of charge migration with and without the CBL revealed its critical role: in CBL-free systems, unregulated charge migration toward

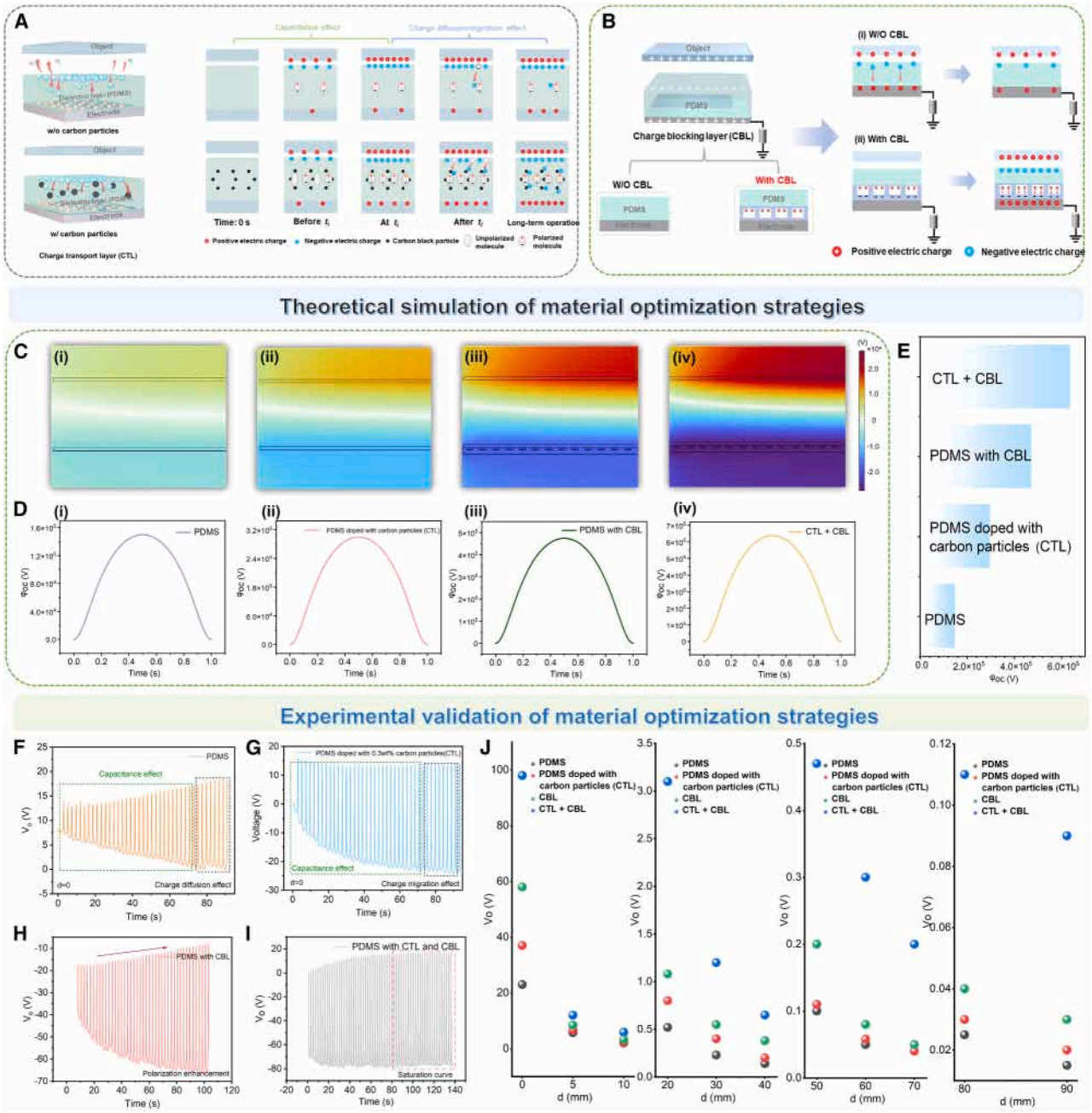

Figure 2. Optimization strategies for high-performance NAES

(A) Schematic illustration of the charge transport mechanism with and without carbon black doping (CTL).

(B) Schematic illustration of the charge transport mechanism of PDMS, both with and without the CBL.

(C) COMSOL simulation of the potential distribution in different dielectric layer configurations: (i) PDMS, (ii) CTL, (iii) PDMS with CBL, and (iv) the synergistic effect of CTL and CBL.

(D) Simulated electrode potential in various dielectric layer configurations: (i) PDMS, (ii) CTL, (iii) PDMS with CBL, and (iv) the synergistic effect of CTL and CBL.

(E) Comparison of the simulated potentials.

(F–I) Experimental validation involved nylon approaching the NAES, with the dielectric layers configured as (F) PDMS, (G) CTL, (H) PDMS with CBL, and (I) a synergistic configuration of CTL and CBL, assessing the output voltage for each configuration.

(J) Comparison of output voltage under different dielectric layer configurations at various approach distances.

electrodes reduced trapping efficiency (Figure 2B). In contrast, the CBL established polarization-stabilized charge traps that harnessed spontaneous polarization fields, enhancing dielectric charge retention and amplifying induced charge density. This optimization minimized charge loss and elevated both retention capacity and perceptual fidelity.

To validate the synergistic roles of the CTL and CBL, we performed theoretical simulations and experimental analyses. COMSOL-based simulations compared electrostatic potential distributions across four dielectric configurations: (1) pristine PDMS, (2) CTL only, (3) PDMS with CBL, and (4) the combined CTL-CBL system (Figure 2C). The combined configuration exhibited the highest potential gradient within the dielectric layer, confirming its superior charge confinement capability. Electrode potential simulations (Figure 2D) further revealed that the CTL-CBL synergy generated the maximum electrode potential difference (Figure 2E), directly correlating with enhanced electrical performance. Experimental validation using nylon as a test substrate corroborated these findings. For pristine PDMS (Figure 2F), the output voltage gradually stabilized due to charge diffusion-limited dynamics. Introducing the carbon-black-doped CTL shifted the dominant mechanism to charge migration, elevating the output voltage via improved capacitance and charge capture efficiency (Figure 2G). To investigate the dispersion morphology of carbon black at different concentrations, photographs of PDMS doped with carbon black were analyzed (Figure S3). These images revealed a gradual darkening of the material as the carbon black concentration increased, visually confirming particle incorporation. SEM images of the samples at different concentrations are provided in Figure S4. At low concentrations, the carbon black particles were evenly dispersed within the PDMS matrix. However, as the concentration increased, a carbon beam began to appear on the surface, indicating that excessive carbon black was difficult to disperse uniformly within the polymer matrix. The impact of the carbon black concentration on the output performance was systematically evaluated (Figure S5). Figure S5A shows the improved charge transport and enhanced capacitive effects with carbon black doping. Figure S5B shows that excessive carbon black concentrations suppressed charge transport due to agglomerate formation, reducing the output voltage. As shown in Figure S5C, 1.1% carbon black is identified as the optimal concentration, balancing dispersion homogeneity and charge transport efficiency. In Figure 2H, the CBL is shown to mitigate excessive charge migration via spontaneous polarization fields, stabilizing bulk charge retention. To optimize the performance of the CBL, we systematically investigated the influence of surface nanostructure parameters. Among various shapes fabricated via photolithography, cylindrical microstructures exhibited the highest output due to their symmetric geometry and uniform field distribution.[43,44] Periodic arrays further enhanced performance by ensuring homogeneous electrostatic environments, as opposed to disordered structures that led to field irregularities.[45] By varying the structural spacing[46] and aspect ratio,[47] we identified an optimal pitch of 40 μm and an aspect ratio of ~2.5, which together maximized charge trapping efficiency and output voltage. These findings confirm that nanostructure geometry critically governs the electrostatic behavior of the CBL and directly impacts sensor performance (Figure S6). Figure S7 shows the analysis of $SrTiO_3$ doping concentrations. High concentrations caused nanoparticle agglomeration, reducing effective trapping sites, whereas low concentrations insufficiently polarized the dielectric. Further investigation of $SrTiO_3$ nanoparticle size is shown in Figure S8: optimal performance occurred at 50 nm, larger particles induced microporous stress fractures, and smaller particles introduced excessive surface defects, compromising stability.

The enhanced performance of the NAES through the synergistic integration of the CTL and CBL, which collectively optimized charge capture and retention, is demonstrated in Figure 2I. The variation in output voltage with distance when using CTLs with different doping concentrations in conjunction with the CBL is shown in Figure S9. The simulated and experimental output voltages exhibit strong agreement (Figure S10), validating not only the fidelity of the finite element model but also supporting the effectiveness of the device architecture in enabling efficient charge transport and electrostatic field coupling. To further substantiate the practical manufacturability of the NAES architecture, we evaluated its fabrication reproducibility and performance consistency through both sample-to-sample and batch-to-batch variation analyses. As shown in Figure S11A, five devices fabricated within the same batch under identical conditions exhibited highly consistent output signals, indicating excellent intra-batch uniformity. Additionally, three independent fabrication batches, each prepared on different days with separately mixed precursor materials, yielded comparable output performance, as demonstrated in Figure S11B. The relative standard deviation of output voltage across all tested samples was below 6%, confirming the robustness and scalability of the fabrication process. These results highlight the high process reliability of NAES, supporting its potential for large-scale integration in wearable and intelligent electronic applications. These results validated the efficacy of the dual-layer design in establishing a robust charge regulation mechanism. Output voltages across dielectric configurations at varying distances were further compared, confirming the superiority of the CTL-CBL architecture in charge modulation (Figure 2J). The environmental robustness of the NAES was underscored through systematic tests. Stable performance under high humidity, attributed to the CTL-CBL charge regulation mechanism, was demonstrated in Figure S12. The dual role of $SrTiO_3$ as a ferroelectric and high-κ material in mitigating temperature-induced charge loss and mechanical stress is highlighted in Figure S13. Light-insensitive operation, attributed to a non-photoelectric mechanism of charge storage and signal generation, is demonstrated in Figure S14. Furthermore, to validate the mechanical stability and structural robustness of the NAES for practical applications, a series of mechanical performance evaluations were conducted. Pressure response measurements revealed that the device generates stable and discernible output voltages within the range of 0–30 kPa, exhibiting excellent repeatability and responsiveness (Figure S15A). This behavior is primarily attributed to the structurally engineered CBL, which enhances contact electrification and charge separation efficiency. Linear fitting results (Figure S15B) show a strong linear relationship between the output voltage and applied pressure, with a high correlation

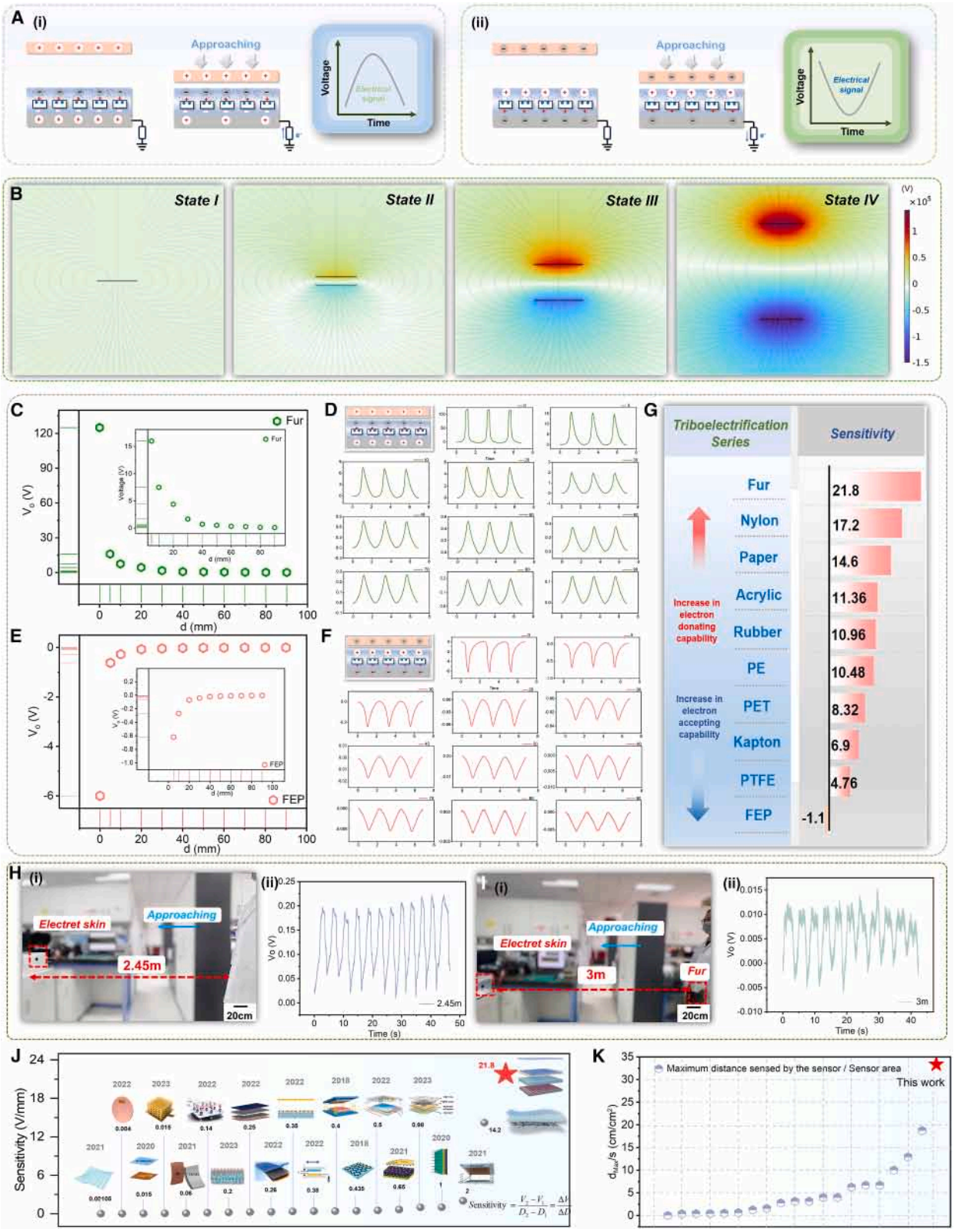

(legend on next page)

coefficient (R^2 > 0.98), indicating superior sensitivity and predictable pressure response. In addition, stress-strain tests (Figure S15C) demonstrated that the NAES can withstand mechanical stress up to 50 kPa without structural failure, highlighting its excellent stretchability and mechanical resilience. Notably, under various strain levels (Figure S15D), the output voltage remained virtually unchanged, indicating that the device maintains stable electrical performance during mechanical deformation. Accelerated aging tests and durability assessments validated long-term stability under extreme temperature/humidity and harsh conditions (Figures S16 and S17). Collectively, these results established the NAES as a universal tele-perception platform, where the CTL-CBL synergy ensured high sensitivity, rapid response, and environmental resilience. Notably, both simulation and experimental results confirmed that this architecture preserved signal fidelity under device miniaturization, further supporting its real-world deployment in adaptive robotics and human-machine interfaces.

The characteristics of the NAES for tele-perception

The working mechanism of the NAES for tele-perception is illustrated in Figure 3A. After pre-charging under high voltage, dielectric polarization was induced in the ferroelectric $SrTiO_3$ nanoparticles embedded within the microstructured PDMS matrix, forming a structured nano-architecture that significantly enhanced the material's electrical responsiveness. When a positively charged object gradually approached, corresponding positive charges accumulated on its surface, triggering a charge induction reaction with the NAES (Figure 3Ai). The degree of polarization on the NAES surface gradually weakened, causing some charges to flow back from the Ni-metal mesh cloth to the reference electrode, balancing the potential until the object's distance changed again. A similar mechanism was observed when a negatively charged object approached (Figure 3Aii). The proximity of the object induced charge migration and polarization effects within the NAES, adjusting the potential distribution between the electrodes and enabling precise detection of the object's position. The COMSOL-simulated potential distribution of the electret skin under different operational states is presented in Figure 3B. These simulations visually reflected the dynamic regulation of the electric field during sensing, displaying potential changes across motion states. In tele-perception experiments, positively charged fur and negatively charged fluorinated ethylene propylene (FEP) were selected as test objects over a distance range of 0–90 mm. The output voltage (V_o) was correlated with the target object's position, allowing accurate tracking of its dynamic positional changes (Figures 3C–3F). To evaluate material adaptability, eight common materials (nylon, polytetrafluoroethylene (PTFE), rubber, paper, acrylic, polyethylene terephthalate [PET], Kapton, and polyethylene [PE]) were tested as perception targets without additional processing (Figure S18).

The experimental results showed that all tested materials could be successfully sensed by the NAES, as detailed in Figure S19. The sensitivity of the NAES to diverse materials was analyzed, with its outstanding performance in high-sensitivity applications highlighted in Figure 3G. The tele-perception capability of the NAES was further validated by accurately detecting a human subject at 2.45 m (Figure 3H). When the subject wore fur, the detection extended to 3 m (Figure 3I), demonstrating practical efficacy. A sensitivity comparison[48–64] between the NAES and prior technologies was conducted, revealing an unprecedented sensitivity record ($\Delta V/\Delta d$ = 21.8; Figure 3J). The relevant device parameters are provided in Figure S20. The maximum sensing distance per unit area was benchmarked against existing systems (Figure 3K), achieving a new record of 30.67 cm/cm^2, with the device parameters listed in Figure S21. These results underscored the NAES's leadership in tele-perception technology and provided a foundation for advancing high-sensitivity sensing applications. The significant miniaturization of the NAES device by reducing its active area to 9 square cm plays a critical role in enhancing its practical applicability across advanced tele-perception scenarios. In modern sensing systems, achieving high sensitivity within a compact footprint is essential for seamless integration into wearable electronics, soft robotics, and autonomous platforms, where space limitations and mechanical flexibility are paramount.[10,65–67] This size reduction not only improves spatial efficiency, as reflected in our normalized sensing distance metric, but also facilitates dense sensor arrays that enable high-resolution spatial mapping and rapid environmental feedback. Moreover, smaller device size reduces mass and power consumption, which is crucial for extending operational lifespan in mobile and aerial platforms. By maintaining or improving sensing performance despite the smaller form factor, the NAES sets a new benchmark in scalable, high-sensitivity tele-perception technologies, opening pathways for deployment in emerging applications requiring compact, lightweight, and precise sensing solutions.

Robust tele-perception HMI in embodied artificial intelligence systems

To comprehensively assess the potential of NAES in embodied artificial intelligence systems, a series of experimental demonstrations were performed, systematically showcasing its performance in diverse HMI scenarios and highlighting its environmental robustness. The NAES was integrated into platforms

Figure 3. Characteristics of tele-perception based on the NAES

(A) Perception mechanism of the NAES for approaching objects that are (i) positively charged and (ii) negatively charged.

(B) COMSOL simulated potential distribution of the NAES under different states.

(C–F) Output voltage of the NAES when (C and D) positively charged fur and (E and F) negatively charged FEP approach the NAES.

(G) Adaptability of the NAES to different materials.

(H) The NAES response when testing the maximum approach distance of a person: (i) human approaching the NAES and (ii) corresponding output voltage.

(I) The NAES response to the maximum approach distance of a person wearing fur: (i) human approaching the NAES and (ii) corresponding output voltage.

(J) Sensitivity comparison between this work and representative studies from the existing literature.

(K) Comparison of the maximum sensing distance per unit area of the NAES between this work and representative studies from the existing literature.

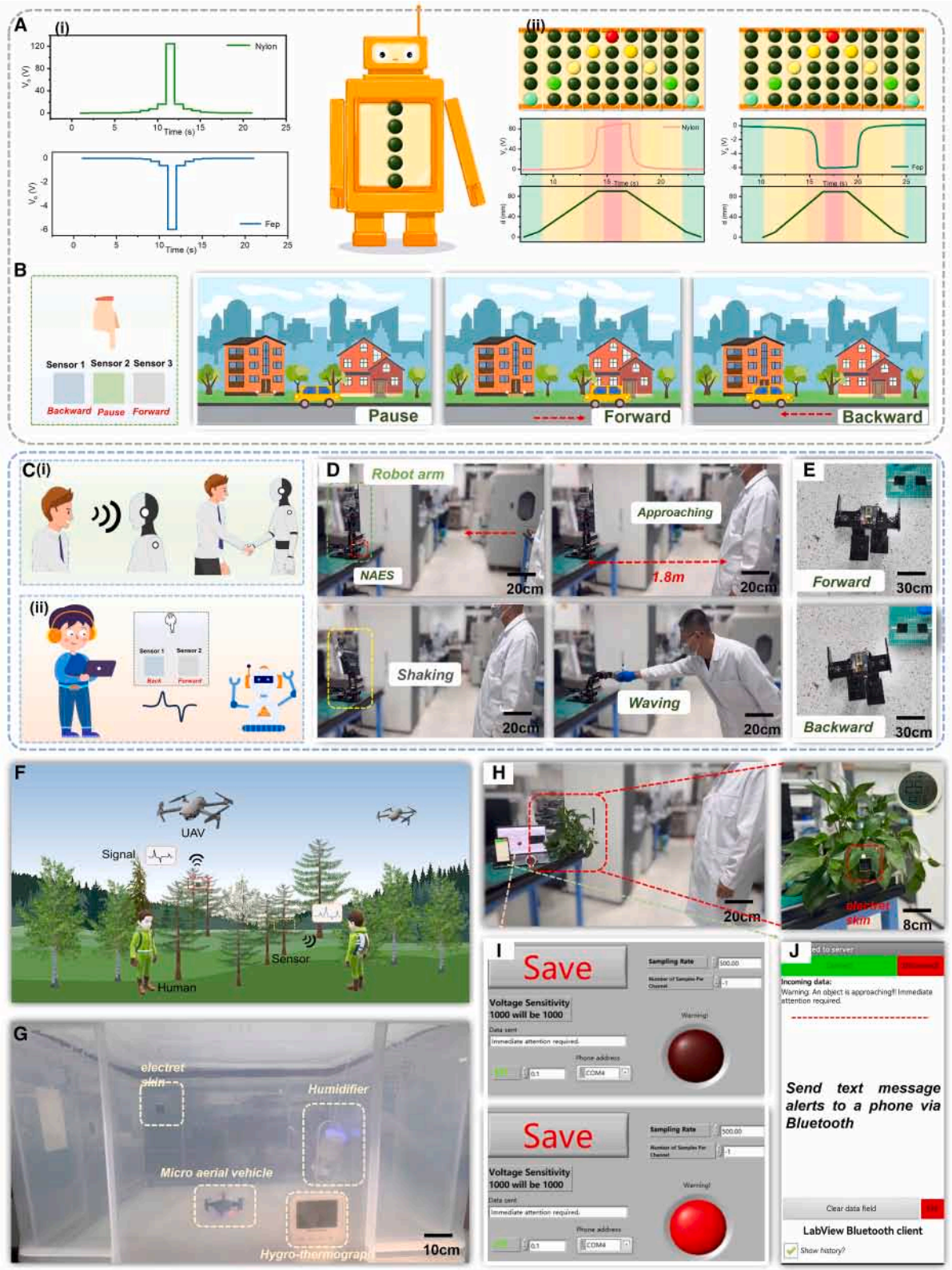

(legend on next page)

with strict dimensional requirements, where its miniaturized design enabled high-performance sensing without compromising range or stability. As a proof of concept, a virtual distance alarm robot HMI was implemented using the NAES, where the output signal corresponded directly to charge density and the proximity of the approaching object. Real-time voltage measurements clearly reflected this relationship as the object advanced (Figure 4A, left). Based on this highly sensitive and stable signal response, a virtual distance warning robot interface was developed using a custom LabVIEW program (Figure 4A, right). This robot was equipped with multiple sets of indicator lights, each triggered by a calibrated threshold voltage (Figure S22; Note S1). Therefore, when the approaching object, such as positively charged nylon or negatively charged FEP, reached the set threshold voltage, the corresponding indicator light was activated (Figure S23). The entire process was fast and accurate and allowed flexible switching of threshold values based on the electronegativity differences of the materials (Video S1). The signal peak polarity (positive or negative) was found to reflect the material's electronegativity, enabling differentiation between materials with varying electronegative properties. For materials with identical electronegativity, the signal amplitude indicated the distance to the target, with larger amplitudes signifying closer proximity. This mechanism not only differentiated material types but also delivered precise spatial information, enhancing the system's ability to estimate material properties and distances.

The demonstration of a car movement system developed through a LabVIEW program is shown in Figure 4B, where the NAES controlled a small vehicle's motion. The system was configured with three independent sensor channels (Figure S24), each assigned distinct thresholds to regulate forward, backward, and stop motions. When a finger remotely approached the NAES, signals were detected in real time, triggering corresponding commands with precision and instant response (Note S2; Video S2). This tele-perception control interface highlighted the NAES's high sensitivity and stability, demonstrating its scalability for practical applications. The application of the NAES in an HMI system was further illustrated (Figure 4C). Initial tests involved interactions with a robotic arm. Upon detecting signals from a nearby human, the NAES transmitted data to an acquisition board, processed via a custom LabVIEW interface. Processed signals were analyzed and relayed as commands to the robotic arm (Figures S25 and S26). As the human approached, the voltage signal increased incrementally. Upon reaching a preset threshold, the system triggered robotic actions such as waving or handshaking (Figure 4D; Video S3). Threshold voltages were adjustable to accommodate diverse approaching objects. A tele-perception control board was developed using LabVIEW to govern robot walking movements (Figure 4E). The system incorporated two independent sensor channels, each with designated thresholds for forward and backward motion. As a finger approached the NAES remotely, signal changes were detected, and corresponding commands were triggered, enabling precise robot control (Note S3; Video S4).

The NAES's robust electrostatic sensing capability enabled remote detection and identification of large, fast-moving objects. Camouflaging the NAES on tree branches to monitor miniature UAV and human activities in outdoor environments was demonstrated (Figure 4F). The operational process for monitoring miniature UAVs and human movements is detailed in Figure S27. A simulation experiment assessing NAES performance in high-humidity environments was conducted (Figure 4G). A transparent enclosure and humidifier were used to simulate high humidity, with the NAES mounted on the enclosure wall and a miniature UAV (Figure S28) placed inside. Thresholds preconfigured via LabVIEW allowed the NAES to detect approaching miniature UAV signals. Similarly, human proximity detection with high sensitivity was validated (Figure 4H). When attached to foliage in high humidity, the NAES detected approaching humans, triggering a LabVIEW alert (Figure 4I) and transmitting Bluetooth notifications to mobile devices (Figure 4J; Video S5). Output voltage variations induced by approaching objects were quantified (Figure S29). The NAES's natural camouflage and moving-object detection capabilities highlighted its potential in smart agriculture, environmental monitoring, and home security. The system exhibited precision and rapid responsiveness even under high humidity, underscoring its stability in complex environments.

Machine learning-empowered somatosensory systems

In the field of embodied perception, achieving both tele-perception of an object's presence and precise classification requires higher demands on system perception performance and intelligent processing. Efficient object identification systems not only require exceptional perception capabilities but also need to leverage advanced technologies, such as deep learning, to accurately extract and infer object features, ensuring robustness and high-precision identification. To address these challenges, we proposed a tele-perception system based on an NAES array, which integrated the powerful capabilities of deep learning to enable real-time, efficient, and precise object

Figure 4. Tele-perception HMI of the NAES

(A) Virtual distance alarm robot: (i) real-time output response of the NAES to external target approach (top: fur, bottom: FEP) and (ii) virtual distance alarm robot based on the NAES.
(B) Demonstration of the car movement interface controlled using the tele-perception control board.
(C) Potential applications of the NAES in intelligent robotic systems.
(D) Demonstration of robotic arm operations when an adult approaches, including waving and handshaking.
(E) Demonstration of robot movement controlled using the tele-perception control board.
(F) Application scenarios of the NAES in complex environments.
(G) Simulation of the NAES's miniature UAV monitoring in a high-humidity environment.
(H) Application scenario of the NAES monitoring human approach.
(I) Alarm function of the tele-perception approach the NAES interface.
(J) The remote approach: the NAES sends SMS alerts to a mobile phone via Bluetooth.

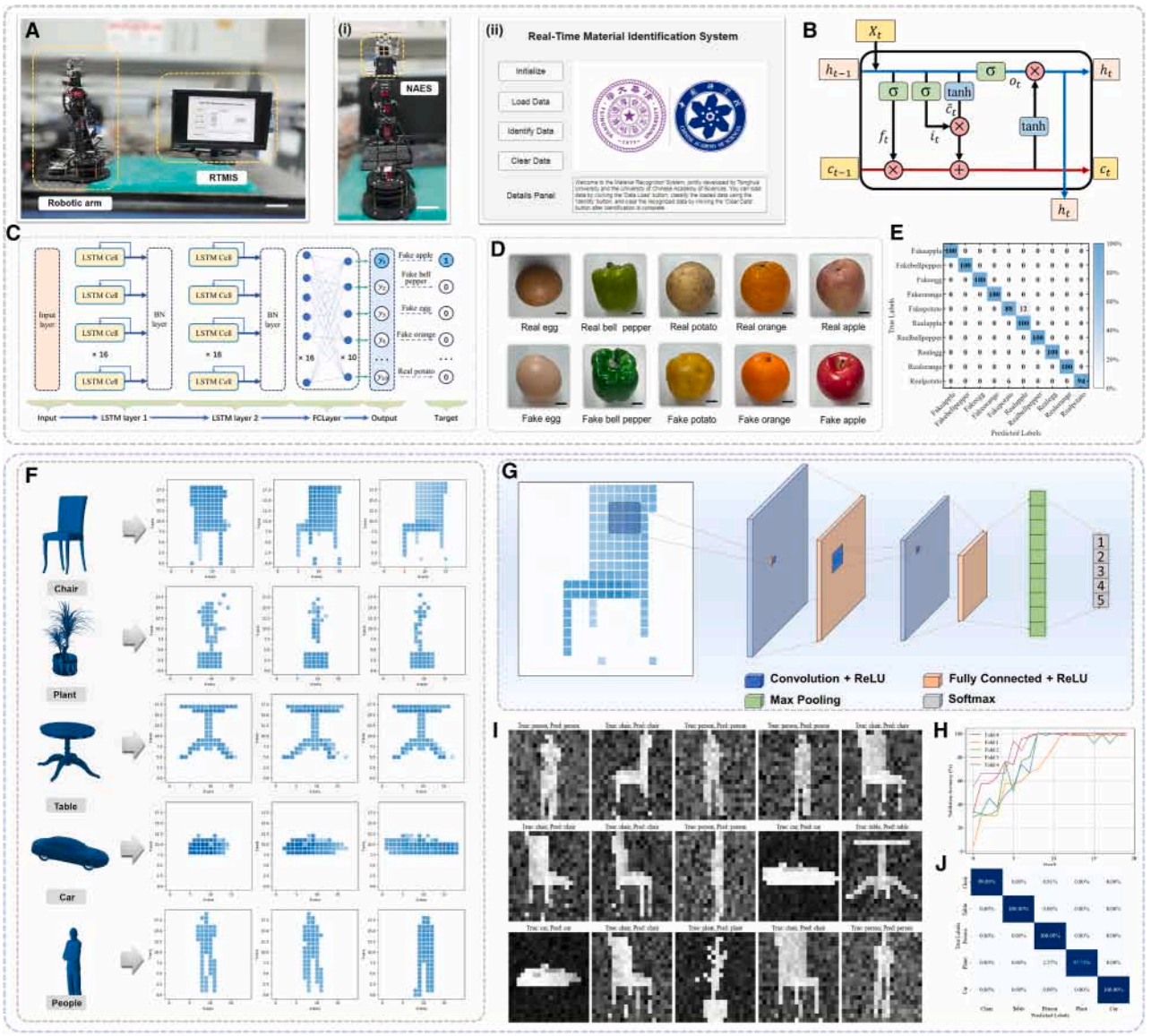

Figure 5. Tele-perception somatosensory system

(A) A photo of a robotic arm with NAES array interacting with RTMIS. (i) A photo of a robotic arm with NAES array. (ii) Homepage of RTMIS.
(B) The structure of the computation unit of LSTM networks.
(C) The overall architecture of the neural network.
(D) The target objects for identification.
(E) The confusion matrix of object identification results under added noise interference.
(F) The 3D object tele-perception system based on NAES matrix (20 × 20 units).
(G) Model architecture of the RTMIS based on a CNN.
(H) Accuracy curves during 5-fold cross-validation training.
(I) Test dataset with added Gaussian noise (standard deviation of 0.5).
(J) Confusion matrix of 5-fold cross-validation.

perception and classification in complex scenarios. Specifically, the NAES array was integrated into a robotic arm, making it the core operational unit for tele-perception. By driving the robotic arm to capture surface feature signals of objects remotely, the system provided technical support for object identification and classification. To validate the practical application of the NAES array, we developed a real-time material identification system (RTMIS) and integrated a long short-term memory (LSTM) deep learning algorithm into the system (Figure 5A). The primary advantage of LSTM lies in its ability to handle sequences of varying lengths, allowing the model to flexibly adapt to datasets with diverse temporal characteristics (Figure 5B).

After training, the model effectively processed input sequences of different lengths. The RTMIS is designed as a fully integrated pipeline that enables seamless transition from data acquisition to signal preprocessing and classification, allowing classification results to be displayed in the mobile application immediately after the sensor contacts the material, without the need for intermediate data storage or manual operation. To ensure low latency, we adopt an efficient pulse segmentation algorithm and a lightweight neural network optimized for real-time inference. Based on 179 test samples, the total signal preprocessing time was 0.161564 s, and the total inference time was 1.681194 s, corresponding to an average processing time of less than 0.01 s per sample on a central processing unit (CPU)-only system. Considering the NAES response time of approximately 0.5 s (Figures S30), the end-to-end latency of the system remains within 1 s, thereby demonstrating its practical real-time capability. To support this real-time functionality, the training process began with preprocessing the raw material data collected by the NAES array, which included segmenting continuous signals and implementing data augmentation (Figures S31 and S32). The data augmentation strategies significantly expanded the dataset size, enhancing the model's training performance. The augmented data were then used to train the neural network, where multiple iterations gradually optimized the model predictions toward actual values.

The overall architecture of the neural network (Figure 5C) consisted of a stacked LSTM with two LSTM layers, each containing 16 units. We designed multi-object identification tasks that included distinguishing between authentic and counterfeit objects such as apples, bell peppers, eggs, oranges, and potatoes, totaling 10 target objects (Figure 5D). The robotic arm, equipped with the NAES array, performed tele-perception of target objects, capturing their electrical signal characteristics in real time based on their material properties. These raw electrical signals were processed into signal curves (Figure S33) and saved as standardized data files. The processed signal curves were subsequently fed into the trained deep learning model, which performed inference and analysis on the signal features to identify the type and authenticity of the objects (Figure S34; Video S6). In standard environments, the system achieved an identification accuracy of 100% (Figure S35). To further evaluate the embodied perception capabilities of the RTMIS under complex conditions, we introduced noise into the test samples to simulate identification challenges in more intricate scenarios. Experimental results indicated that the system maintained an accuracy of 98.32% even under significant interference (Figure 5E), showcasing its excellent stability and high-performance reliability in dynamic and challenging environments. Our work presents a holistic innovation in intelligent material perception by integrating three key advancements: a passive and energy-efficient electrostatic sensing mechanism, system-level integration from sensing to classification, and temporal modeling using deep learning. Unlike prior triboelectric nanogenerators (TENGs) or ultrasonic systems that rely on physical contact or active signal emission, our NAES array enables non-contact material perception with high spatial resolution through electrostatic field detection. The multilayer sensor design, incorporating both charge transport and blocking layers, enhances sensitivity and environmental robustness. Building upon this foundation, we implement a fully integrated neuromorphic framework with a stacked LSTM network that directly processes raw time-series signals, capturing subtle temporal patterns without manual feature engineering. This architecture supports real-time, end-to-end classification and demonstrates strong adaptability to signal variability and class similarity. In comparison to prior TENG-based sensors,[68,69] which lack temporal modeling and require physical contact, and ultrasonic systems,[70,71] which are power intensive and less scalable, our approach delivers a passive, parallelizable, and intelligent sensing solution. These combined innovations significantly enhance system robustness, scalability, and applicability in realistic, complex identification tasks, marking a distinct advancement over existing technologies.

The NAES array exhibited exceptional high-precision object identification capabilities and remarkable scalability. To achieve this, a 4×4 NAES sensing matrix was designed, and the effectiveness of the shielding layer in mitigating electrostatic interference was validated by comparing results with and without the shielding layer (Figures S36 and S37). To extend the validated sensing capabilities of the system beyond static object recognition, we carried out remote material mapping experiments using acrylic targets with well-defined geometries, namely the letters C, O, and L. To introduce material diversity, thin films of PTFE, Kapton, and bare acrylic were applied to their surfaces. The entire mapping procedure was executed using a LabVIEW-based control program, which enabled precise trajectory planning and synchronized data acquisition (Figure S38A). During the mapping process, the NAES system performed non-contact scanning by approaching and retracting from the targets within a distance of approximately 5–10 cm, continuously collecting spatial data (Figure S38B). The reconstructed material-specific maps, as presented in Figure S38C and Video S7, clearly reveal both the geometric outlines and material differences, with red, green, and blue representing PTFE, Kapton, and acrylic, respectively. The signal intensity varies with the sensor's distance from the target, enabling depth-aware perception. These results confirm that the NAES system can effectively identify materials based on their intrinsic signal responses, even when applied to geometrically similar substrates. Compared with previous techniques such as TENGs and compact ultrasonic arrays, our system exhibits advantages in spatial resolution, scalability, and passive sensing. Furthermore, the neuromorphic multi-array design supports parallel data processing, enhancing real-time interactions with the environment. This work demonstrates that the NAES system not only distinguishes materials based on peak signal differences but also constructs high-fidelity spatial material maps, highlighting its potential for intelligent tele-perception and autonomous material classification in practical applications.

In addition, to validate its functionality in real-world scenarios, the NAES array was employed to scan real objects, and the collected electrical signal data were input into a convolutional neural network (CNN) model to achieve accurate object identification and classification. The CNN algorithm, known for its strength in extracting spatial features, effectively captured critical information from multidimensional data, thereby enhancing

the accuracy and stability of tele-perception. To further validate the system's tele-perception capabilities, we constructed a 20 × 20 NAES array and evaluated its potential applications in three-dimensional object perception by scanning three-dimensional objects in a simulated environment. This comprehensive sensing approach enabled full three-dimensional tele-perception and analysis, significantly improving identification performance and providing robust technical support for applications in more complex scenarios. During object identification, the electrical signal responses varied according to the material properties of the objects. To address this, a material weighting coefficient was introduced based on the electrical signal strengths observed in experiments (Figure S39), which enhanced the precision and sensitivity of the sensing system. Five objects identified by the NAES array are illustrated in Figure 5F: a chair, a plant, a table, a car, and a human. The CNN architecture trained on this dataset is shown in Figure 5G. It consisted of two convolutional layers and two fully connected layers. The first convolutional layer included 8 channels, each using a 1 × 3 × 3 kernel. After pooling and activation, an 8 × 10 × 10 feature map was generated. The second convolutional layer also had 8 channels, each using an 8 × 3 × 3 kernel, producing an 8 × 5 × 5 feature map after pooling and activation. The extracted feature maps were flattened and passed to the first fully connected layer (200 × 32). Following activation, a 32-dimensional feature vector was produced, which was then input into the second fully connected layer (32 × 5) to output classification results. The output layer contained 5 neurons, and the predicted category was determined by the neuron with the highest value. To validate system performance, 687 sample data points were simulated, with 50% used for training and 50% for testing. To assess the system's embodied perception capabilities under challenging conditions, Gaussian noise with a mean of 0 and a standard deviation of 0.5 was introduced to the original data during the simulation process to simulate noise interference and data acquisition errors in complex environments. During the 5-fold cross-validation training process, we plotted the validation accuracy curves for each fold (Figure 5H). The curves for fold0 to fold4 all demonstrated favorable convergence trends, indicating that the model was able to learn stably and progressively improve its performance on the validation sets throughout the training process. Following training, we further evaluated the model using a noisy dataset designed to simulate real-world signal interference (Figure 5I), thereby assessing its robustness under practical application conditions. To provide a comprehensive evaluation of the model's performance across all 5 folds, we aggregated the test set predictions from each fold and computed a consolidated confusion matrix. Specifically, we preserved the individual test results from each fold and subsequently calculated an overall classification accuracy of 99.42%. The resulting confusion matrix (Figure 5J) visually summarizes the classification outcomes across all test samples, offering a holistic view of the model's predictive capabilities when integrated across multiple iterations of cross-validation. The results, presented in Figure 5J, indicate that the system achieved 100% classification accuracy on the tested dataset. This exceptional performance underscored the successful integration of the NAES array with deep learning technology, enabling real-time and efficient object identification. By combining advanced sensor technology with deep learning algorithms, the system demonstrated significant potential for embodied perception in the field of tele-perception. The fusion of these technologies facilitated multidimensional data acquisition and high-precision signal analysis, allowing the system to quickly adapt to complex scenarios and diverse object types.

DISCUSSION

In summary, the NAES system, anchored in a meta-structured heterointerface, represents a paradigm shift in tele-perception for embodied artificial intelligence. By integrating the CTL and CBL, this architecture enables the first successful transition from surface-confined charge retention to bulk charge trapping, effectively resolving the chronic trade-off between sensing range and environmental robustness. Experimental validation and COMSOL simulations confirm a 3-m perception range ($\Delta V/\Delta d$ = 21.8), with stability maintained under humidity fluctuations and Gaussian noise challenges that cripple conventional infrared, capacitive, and ultrasonic sensors. The meta-structured electret heterointerface is pivotal in enabling electroreceptor-based tele-perception, where the CTL enables charge redistribution through conductive percolation networks, while the CBL leverages ferroelectric polarization to trap bulk electrostatic charge. The NAES's advanced capabilities facilitate resilient HMIs, enabling precise control of robot movement and miniature UAVs in conditions of high darkness and high humidity. In addition, this unique architecture enables non-contact, non-visual, and non-acoustic tele-perception with high environmental robustness by minimizing external interference in charge transport and integrating advanced algorithms, thereby ensuring stable and adaptive operation in dark, humid, and visually occluded conditions. This establishes a closed-loop tele-perception→interact framework, replacing the traditional approach-→touch→interact model. The NAES pioneers a universal charge-trapping paradigm with implications for remote control and neuromorphic computing. Future integration with advanced algorithms and cross-modal data fusion architectures promises to unlock nanosecond-level decision-making for adaptive tele-perception in embodied intelligence, catalyzing tactile-free human-machine symbiosis. These capabilities redefine the boundaries of wearable sensing, enabling transformative applications in intelligent HMIs, autonomous robotics, and adaptive healthcare wearables for real-time physiological monitoring in complex environments. It heralds a future of context-aware, self-adapting systems that seamlessly interface with dynamic environments, positioning itself as a linchpin of next-generation cyber-physical ecosystems.

METHODS

Materials

Silicon wafers, PDMS, curing agent, $SrTiO_3$ powders, carbon black powder, and the Ni-metal mesh were all commercially sourced and used without further purification.

Fabrication of a CBL using carbon-black-doped PDMS

The PDMS base and curing agent were mixed in a 10:1 ratio, and an appropriate amount of carbon black was measured and added based on the desired percentage. The carbon black was then thoroughly dispersed in solution using a magnetic stirrer or ultrasonic disperser to ensure uniform distribution. The dispersed carbon black solution was gradually added to the PDMS and curing agent mixture, followed by thorough mixing using a high-speed stirrer or stirring rod. The resulting mixture was placed in a vacuum chamber for degassing, typically for 10–15 min, until all surface bubbles were eliminated. Afterward, the mixture was spin coated to form a thin film and cured in a vacuum oven at 60°C.

Fabrication of silicon wafer templates

Initially, a layer of photoresist was applied to silicon wafer substrates. Selective exposure of the photoresist was achieved through UV exposure using a mask. Subsequently, the exposed areas were dissolved using a developer solution, revealing the pattern from the mask on the photoresist. A selective etching process was carried out on the substrate using inductively coupled plasma (ICP) etching. The remaining photoresist protected the substrate from alteration during these processes. After etching, the photoresist was removed using N-methylpyrrolidone (NMP) to obtain microstructured templates.

Fabrication of a CBL with structured ferroelectricity nanoparticle doping

Using optimal parameters as an example, we (1) weighed 0.12 g of $SrTiO_3$ inorganic nonmetal nanoparticles; (2) mixed $SrTiO_3$ inorganic nonmetal nanoparticles with 10 mL of ethanol and ultrasonicated them for 20 min to form a homogeneous suspension; (3) added 1 mL PDMS precursor to the $SrTiO_3$ ethanol suspension and stirred for 10 min; (4) placed the mixture in an oven at 90°C for over 10 h to ensure complete evaporation of ethanol; (5) added the curing agent and stirred the mixture for 5 min; (6) poured the mixture of $SrTiO_3$ inorganic nonmetal nanoparticles and PDMS onto the microstructured PDMS film; and (7) cured the composite material in an oven at 80°C for 3 h. Thus, a composite film with structured doping of inorganic nonmetal nanoparticles was prepared.

Manufacture of the NAES

The NAES based on structured nanocomposites was successfully fabricated by bonding a plasma-treated carbon-black-doped PDMS film, a PDMS film structured with inorganic nonmetallic nanoparticle doping, and the Ni-metal mesh.

Electric measurement and characterization

A linear motor (LinMotS01-72/500) was employed to control the distance between objects and the NAES. The SEM images were obtained by a scanning electron microscope (Nova Nano SEM 450). Plasma cleaner provided voltage for the pre-charging process. The open-circuit voltage was measured using a programmable electrostatic voltmeter (Keithley 6514). For basic output performance testing of the NAES, a programmable electrostatic voltmeter (Keithley 6514) was directly connected to a synchronized data acquisition card (National Instruments 6346) to measure multi-channel voltage signals. A robotic arm with the NAES was used to execute remote approach commands. A multi-channel data acquisition program developed on the LabVIEW platform was used for data collection, processing, and storage.

RESOURCE AVAILABILITY

Lead contact

Further information and requests for resources and reagents should be directed to and will be fulfilled by the lead contact, Di Wei (dw344@cam.ac.uk).

Materials availability

The materials used in this study are available from the corresponding authors upon reasonable request.

Data and code availability

All data generated during this study are included in the article and supplemental information.

ACKNOWLEDGMENTS

This work was supported by the Beijing Natural Science Foundation (grant no. IS23040).

AUTHOR CONTRIBUTIONS

D.W. and Z.L.W. proposed the idea and the project. D.W. designed all the experiments and supervised the whole project. Y.D. carried out the experiments in this paper. P.S., H.L., and T.R. provided support for the data algorithm. Z.Z. provided support for theoretical simulations. Y.D., P.S., F.Y., and D.C. analyzed the corresponding data. All authors discussed the results and commented on the manuscript. D.W. and Y.D. wrote this paper.

DECLARATION OF INTERESTS

The authors declare no conflicts of interest.

SUPPLEMENTAL INFORMATION

Supplemental information can be found online at https://doi.org/10.1016/j.matt.2025.102363.

Received: March 23, 2025
Revised: June 16, 2025
Accepted: July 9, 2025
Published: August 5, 2025

REFERENCES

1. Gupta, A., Savarese, S., Ganguli, S., and Fei-Fei, L. (2021). Embodied intelligence via learning and evolution. Nat. Commun. *12*, 5721. https://doi.org/10.1038/s41467-021-25874-z.
2. Barreiros, J.A., Xu, A., Pugach, S., Iyengar, N., Troxell, G., Cornwell, A., Hong, S., Selman, B., and Shepherd, R.F. (2022). Haptic perception using optoelectronic robotic flesh for embodied artificially intelligent agents. Sci. Robot. *7*, eabi6745. https://doi.org/10.1126/scirobotics.abi6745.
3. Nitzan, M., Casadiego, J., and Timme, M. (2017). Revealing physical interaction networks from statistics of collective dynamics. Sci. Adv. *3*, e1600396. https://doi.org/10.1126/sciadv.1600396.
4. Peng, Q., Long, C.L., Malhotra, S., and Humphrey, M.B. (2013). A Physical Interaction Between the Adaptor Proteins DOK3 and DAP12 Is Required to Inhibit Lipopolysaccharide Signaling in Macrophages. Sci. Signal. *6*, ra72. https://doi.org/10.1126/scisignal.2003801.
5. Du, Y., Shen, P., Liu, H., Zhang, Z., Ren, T., Shi, R., Wang, Z., and Wei, D. (2024). Conformal Self-Powered Inertial Displacement Sensor with

Geometric Optimization for In Situ Noninvasive Data Acquisition. Adv. Funct. Mater. *34*, 2409602. https://doi.org/10.1002/adfm.202409602.

6. Jang, Y.-W., Kim, J., Shin, J., Jo, J.-W., Shin, J.W., Kim, Y.-H., Cho, S.W., and Park, S.K. (2024). Autonomous Artificial Olfactory Sensor Systems with Homeostasis Recovery via a Seamless Neuromorphic Architecture. Adv. Mater. *36*, 2400614. https://doi.org/10.1002/adma.202400614.
7. Ding, S., Saha, T., Yin, L., Liu, R., Khan, M.I., Chang, A.-Y., Lee, H., Zhao, H., Liu, Y., Nazemi, A.S., et al. (2024). A fingertip-wearable microgrid system for autonomous energy management and metabolic monitoring. Nat. Electron. *7*, 788–799. https://doi.org/10.1038/s41928-024-01236-7.
8. Zhu, M., Sun, Z., Zhang, Z., Shi, Q., He, T., Liu, H., Chen, T., and Lee, C. (2020). Haptic-feedback smart glove as a creative human-machine interface (HMI) for virtual/augmented reality applications. Sci. Adv. *6*, eaaz8693. https://doi.org/10.1126/sciadv.aaz8693.
9. Zhong, M., Zhang, L., Liu, X., Zhou, Y., Zhang, M., Wang, Y., Yang, L., and Wei, D. (2021). Wide linear range and highly sensitive flexible pressure sensor based on multistage sensing process for health monitoring and human-machine interfaces. Chem. Eng. J. *412*, 128649. https://doi.org/10.1016/j.cej.2021.128649.
10. Cheng, A., Li, X., Li, D., Chen, Z., Cui, T., Tao, L.-Q., Jian, J., Xiao, H., Shao, W., Tang, Z., et al. (2025). An intelligent hybrid-fabric wristband system enabled by thermal encapsulation for ergonomic human-machine interaction. Nat. Commun. *16*, 591. https://doi.org/10.1038/s41467-024-55649-1.
11. Nguyen, D.T., Zeng, Q., Tian, X., Chia, P., Wu, C., Liu, Y., and Ho, J.S. (2024). Ambient health sensing on passive surfaces using metamaterials. Sci. Adv. *10*, eadj6613. https://doi.org/10.1126/sciadv.adj6613.
12. Batarseh, M., Sukhov, S., Shen, Z., Gemar, H., Rezvani, R., and Dogariu, A. (2018). Passive sensing around the corner using spatial coherence. Nat. Commun. *9*, 3629. https://doi.org/10.1038/s41467-018-05985-w.
13. Nelidova, D., Morikawa, R.K., Cowan, C.S., Raics, Z., Goldblum, D., Scholl, H.P.N., Szikra, T., Szabo, A., Hillier, D., and Roska, B. (2020). Restoring light sensitivity using tunable near-infrared sensors. Science *368*, 1108–1113. https://doi.org/10.1126/science.aaz5887.
14. Xu, Y., Xu, X., Huang, Y., Tian, Y., Cheng, M., Deng, J., Xie, Y., Zhang, Y., Zhang, P., Wang, X., et al. (2024). Gate-Tunable Positive and Negative Photoconductance in Near-Infrared Organic Heterostructures for In-Sensor Computing. Adv. Mater. *36*, 2402903. https://doi.org/10.1002/adma.202402903.
15. He, H., Liu, J., Wang, Y., Zhao, Y., Qin, Y., Zhu, Z., Yu, Z., and Wang, J. (2022). An Ultralight Self-Powered Fire Alarm e-Textile Based on Conductive Aerogel Fiber with Repeatable Temperature Monitoring Performance Used in Firefighting Clothing. ACS Nano *16*, 2953–2967. https://doi.org/10.1021/acsnano.1c10144.
16. Du, Y., Tang, Q., He, W., Liu, W., Wang, Z., Wu, H., Li, G., Guo, H., Li, Z., Peng, Y., and Hu, C. (2021). Harvesting ambient mechanical energy by multiple mode triboelectric nanogenerator with charge excitation for self-powered freight train monitoring. Nano Energy *90*, 106543. https://doi.org/10.1016/j.nanoen.2021.106543.
17. Bühling, B., Maack, S., and Strangfeld, C. (2024). Fluidic Ultrasound Generation for Non-Destructive Testing. Adv. Mater. *36*, 2311724. https://doi.org/10.1002/adma.202311724.
18. Qiu, C., Zhang, Z., Xu, Z., Qiao, L., Ning, L., Zhang, S., Su, M., Wu, W., Song, K., Xu, Z., et al. (2024). Transparent ultrasonic transducers based on relaxor ferroelectric crystals for advanced photoacoustic imaging. Nat. Commun. *15*, 10580. https://doi.org/10.1038/s41467-024-55032-0.
19. Aksnes, D.L., Røstad, A., Kaartvedt, S., Martinez, U., Duarte, C.M., and Irigoien, X. Light penetration structures the deep acoustic scattering layers in the global ocean. Sci. Adv. 3, e1602468. https://doi.org/10.1126/sciadv.1602468.
20. Tang, H.-b., Hao, Y.-f., Hu, G.-y., Lu, Q.-m., Ren, C., Zhang, Y., Guo, A., Hu, P., Wang, Y.-l., Wang, X.-b., et al. (2025). Laboratory observation of ion drift acceleration via reflection off laser-produced magnetized collisionless shocks. Sci. Adv. *11*, eadn3320. https://doi.org/10.1126/sciadv.adn3320.
21. Yang, L., Chen, X., Dutta, A., Zhang, H., Wang, Z., Xin, M., Du, S., Xu, G., and Cheng, H. (2025). Thermoelectric porous laser-induced graphene-based strain-temperature decoupling and self-powered sensing. Nat. Commun. *16*, 792. https://doi.org/10.1038/s41467-024-55790-x.
22. Casciati, F., and Wu, L. (2013). Local positioning accuracy of laser sensors for structural health monitoring. Struct. Control Health Monit. *20*, 728–739. https://doi.org/10.1002/stc.1488.
23. Lee, C.-L., Chen, Y.-T., Su, R.K.L., and Wang, Y.-P. (2023). Active Microvibration Control of Tool Platforms Installed on the Floors Subjected to Moving Vehicles in Industrial Factories. Struct. Control Health Monit. *2023*, 1–19. https://doi.org/10.1155/2023/2077180.
24. Laflamme, S., Kollosche, M., Connor, J.J., and Kofod, G. (2012). Soft capacitive sensor for structural health monitoring of large-scale systems. Struct. Control Health Monit. *19*, 70–81. https://doi.org/10.1002/stc.426.
25. He, X., Zhang, B., Liu, Q., Chen, H., Cheng, J., Jian, B., Yin, H., Li, H., Duan, K., Zhang, J., and Ge, Q. (2024). Highly conductive and stretchable nanostructured ionogels for 3D printing capacitive sensors with superior performance. Nat. Commun. *15*, 6431. https://doi.org/10.1038/s41467-024-50797-w.
26. Qin, R., Hu, M., Li, X., Liang, T., Tan, H., Liu, J., and Shan, G. (2021). A new strategy for the fabrication of a flexible and highly sensitive capacitive pressure sensor. Microsyst. Nanoeng. *7*, 100. https://doi.org/10.1038/s41378-021-00327-1.
27. Kondo, M., Melzer, M., Karnaushenko, D., Uemura, T., Yoshimoto, S., Akiyama, M., Noda, Y., Araki, T., Schmidt, O.G., and Sekitani, T. (2020). Imperceptible magnetic sensor matrix system integrated with organic driver and amplifier circuits. Sci. Adv. *6*, eaay6094. https://doi.org/10.1126/sciadv.aay6094.
28. Yan, Y., Hu, Z., Yang, Z., Yuan, W., Song, C., Pan, J., and Shen, Y. (2021). Soft magnetic skin for super-resolution tactile sensing with force self-decoupling. Sci. Robot. *6*, eabc8801. https://doi.org/10.1126/scirobotics.abc8801.
29. Xu, R., Cañón Bermúdez, G.S., Pylypovskyi, O.V., Volkov, O.M., Oliveros Mata, E.S., Zabila, Y., Illing, R., Makushko, P., Milkin, P., Ionov, L., et al. (2022). Self-healable printed magnetic field sensors using alternating magnetic fields. Nat. Commun. *13*, 6587. https://doi.org/10.1038/s41467-022-34235-3.
30. Griffin, C., Duller, R.A., and Straub, K.M. (2023). The degradation and detection of environmental signals in sediment transport systems. Sci. Adv. *9*, eadi8046. https://doi.org/10.1126/sciadv.adi8046.
31. LaBarbera, M. (1990). Principles of Design of Fluid Transport Systems in Zoology. Science *249*, 992–1000. https://doi.org/10.1126/science.2396104.
32. Watts, S. (2010). Optical microchip sensors. Nat. Photonics *4*, 433–434. https://doi.org/10.1038/nphoton.2010.150.
33. Zhu, H., Shao, B., Shen, Z., You, S., Yin, J., Wehbe, N., Wang, L., Song, X., Abulikemu, M., Basaheeh, A., et al. (2025). In situ energetics modulation enables high-efficiency and stable inverted perovskite solar cells. Nat. Photonics *19*, 28–35. https://doi.org/10.1038/s41566-024-01542-8.
34. (2000). High-Speed Light Modulation. Science *290*, 2213. https://doi.org/10.1126/science.290.5500.2213a.
35. Guo, Z.H., Wang, H.L., Shao, J., Shao, Y., Jia, L., Li, L., Pu, X., and Wang, Z.L. (2022). Bioinspired soft electroreceptors for artificial precontact somatosensation. Sci. Adv. *8*, eabo5201. https://doi.org/10.1126/sciadv.abo5201.

36. Du, Y., Shen, P., Liu, H., Zhang, Y., Jia, L., Pu, X., Yang, F., Ren, T., Chu, D., Wang, Z., and Wei, D. (2024). Multi-receptor skin with highly sensitive tele-perception somatosensory. Sci. Adv. *10*, eadp8681. https://doi.org/10.1126/sciadv.adp8681.

37. Masuda, R. (1986). Multifunctional optical proximity sensor using phase modulation. JRoS *3*, 137–147. https://doi.org/10.1002/rob.4620030203.

38. Koerfer, K., Watson, T., and Lappe, M. (2024). Inability to pursue nonrigid motion produces instability of spatial perception. Sci. Adv. *10*, eadp6204. https://doi.org/10.1126/sciadv.adp6204.

39. Alqahtani, J., Sangtarash, S., and Sadeghi, H. (2023). Influence of Environmental Fluctuations on Quantum Interference in Naphthalene and Azulene. Small Sci. *3*, 2300075. https://doi.org/10.1002/smsc.202300075.

40. Li, R., Wei, D., and Wang, Z. (2024). Synergizing Machine Learning Algorithm with Triboelectric Nanogenerators for Advanced Self-Powered Sensing Systems. Nanomaterials *14*, 165. https://doi.org/10.3390/nano14020165.

41. Mutz, J., Iniesta, R., and Lewis, C.M. (2024). Metabolomic age (MileAge) predicts health and life span: A comparison of multiple machine learning algorithms. Sci. Adv. *10*, eadp3743. https://doi.org/10.1126/sciadv.adp3743.

42. Du, Y., Wang, Z., and Wei, D. (2025). Advancing tele-perception: a paradigm shift from traditional non-contact sensing to adaptive embodied artificial intelligence systems. Sci. Bull. *70*, 1375–1379. https://doi.org/10.1016/j.scib.2025.02.014.

43. Kisomi, M.K., Roomi, M.S., and Mahmud, M.A.P. (2024). Mode-Adaptive Surface Pattern Design for Enhanced Triboelectric Nanogenerator Performance. Nanoenergy Advances *4*, 328–343. https://doi.org/10.3390/nanoenergyadv4040020.

44. Xia, Z., Feng, P.-Y., Jing, X., Li, H., Mi, H.-Y., and Liu, Y. (2021). Design and Optimization Principles of Cylindrical Sliding Triboelectric Nanogenerators. Micromachines *12*, 567. https://doi.org/10.3390/mi12050567.

45. Gao, L., Li, J., Wang, Z., Bu, M., Zhai, L., Wu, S., Hu, N., Dai, K., Wu, L., Lee, A., and Mu, X. (2022). A high performance triboelectric nanogenerator based on ordered doping technique for human-machine interaction sensing. Nano Energy *95*, 107025. https://doi.org/10.1016/j.nanoen.2022.107025.

46. Pradel, K.C., and Fukata, N. (2021). Systematic optimization of triboelectric nanogenerator performance through surface micropatterning. Nano Energy *83*, 105856. https://doi.org/10.1016/j.nanoen.2021.105856.

47. Xi, Y., Zhang, F., and Shi, Y. (2021). Effects of surface micro-structures on capacitances of the dielectric layer in triboelectric nanogenerator: A numerical simulation study. Nano Energy *79*, 105432. https://doi.org/10.1016/j.nanoen.2020.105432.

48. Yuan, F., Liu, S., Zhou, J., Wang, S., Wang, Y., Xuan, S., and Gong, X. (2021). Smart touchless triboelectric nanogenerator towards safeguard and 3D morphological awareness. Nano Energy *86*, 106071. https://doi.org/10.1016/j.nanoen.2021.106071.

49. Peng, S., Feng, Y., Liu, Y., Feng, M., Wu, Z., Cheng, J., Zhang, Z., Liu, Y., Shen, R., and Wang, D. (2022). New blind navigation sensor based on triboelectrification and electrostatic induction. Nano Energy *104*, 107899. https://doi.org/10.1016/j.nanoen.2022.107899.

50. Xi, Y., Hua, J., and Shi, Y. (2020). Noncontact triboelectric nanogenerator for human motion monitoring and energy harvesting. Nano Energy *69*, 104390. https://doi.org/10.1016/j.nanoen.2019.104390.

51. Wang, B., Gao, M., Fu, X., Geng, M., Liu, Y., Cheng, N., Li, J., Li, L., Zhang, Z., and Song, Y. (2023). 3D printing deep-trap hierarchical architecture-based non-contact sensor for multi-direction motion monitoring. Nano Energy *107*, 108135. https://doi.org/10.1016/j.nanoen.2022.108135.

52. Anaya, D.V., Zhan, K., Tao, L., Lee, C., Yuce, M.R., and Alan, T. (2021). Contactless tracking of humans using non-contact triboelectric sensing technology: Enabling new assistive applications for the elderly and the visually impaired. Nano Energy *90*, 106486. https://doi.org/10.1016/j.nanoen.2021.106486.

53. Hou, Z., Liu, T., Li, M., Xu, Y., Wu, X., Luo, S., Cai, C., Mou, Y., Qiu, Y., Nie, S., and Lu, D. (2024). Superhydrophobic Triboelectric Structural Materials Enabled by Hierarchical Spatial Assembly. Adv. Funct. Mater. *34*, 2400750. https://doi.org/10.1002/adfm.202400750.

54. Zhao, C., Wang, Z., Wang, Y., Qian, Z., Tan, Z., Chen, Q., Pan, X., Xu, M., and Lai, Y.C. (2023). MXene-Composite-Enabled Ultra-long-Distance Detection and Highly Sensitive Self-Powered Noncontact Triboelectric Sensors and Their Applications in Intelligent Vehicle Perception. Adv. Funct. Mater. *33*, 2306381. https://doi.org/10.1002/adfm.202306381.

55. Salauddin, M., Rana, S.S., Sharifuzzaman, M., Lee, S.H., Zahed, M.A., Do Shin, Y., Seonu, S., Song, H.S., Bhatta, T., and Park, J.Y. (2022). Laser-carbonized MXene/ZiF-67 nanocomposite as an intermediate layer for boosting the output performance of fabric-based triboelectric nanogenerator. Nano Energy *100*, 107462. https://doi.org/10.1016/j.nanoen.2022.107462.

56. Shrestha, K., Sharma, S., Pradhan, G.B., Bhatta, T., Maharjan, P., Rana, S.S., Lee, S., Seonu, S., Shin, Y., and Park, J.Y. (2022). A Siloxene/Ecoflex Nanocomposite-Based Triboelectric Nanogenerator with Enhanced Charge Retention by MoS2/LIG for Self-Powered Touchless Sensor Applications. Adv. Funct. Mater. *32*, 2113005. https://doi.org/10.1002/adfm.202113005.

57. Cao, J., Fu, X., Zhu, H., Qu, Z., Qi, Y., Zhang, Z., Zhang, Z., Cheng, G., Zhang, C., and Ding, J. (2022). Self-Powered Non-Contact Motion Vector Sensor for Multifunctional Human–Machine Interface. Small Methods *6*, e2200588. https://doi.org/10.1002/smtd.202200588.

58. Guo, H., Jia, X., Liu, L., Cao, X., Wang, N., and Wang, Z.L. (2018). Free-standing Triboelectric Nanogenerator Enables Noncontact Motion-Tracking and Positioning. ACS Nano *12*, 3461–3467. https://doi.org/10.1021/acsnano.8b00140.

59. Tang, Y., Zhou, H., Sun, X., Diao, N., Wang, J., Zhang, B., Qin, C., Liang, E., and Mao, Y. (2019). Triboelectric Touch-Free Screen Sensor for Noncontact Gesture Recognizing. Adv. Funct. Mater. *30*. https://doi.org/10.1002/adfm.201907893.

60. Zhang, W., Lu, Y., Liu, T., Zhao, J., Liu, Y., Fu, Q., Mo, J., Cai, C., and Nie, S. (2022). Spheres Multiple Physical Network-Based Triboelectric Materials for Self-Powered Contactless Sensing. Small *18*, e2200577. https://doi.org/10.1002/smll.202200577.

61. Rana, S.M.S., Zahed, M.A., Rahman, M.T., Salauddin, M., Lee, S.H., Park, C., Maharjan, P., Bhatta, T., Shrestha, K., and Park, J.Y. (2021). Cobalt-Nanoporous Carbon Functionalized Nanocomposite-Based Triboelectric Nanogenerator for Contactless and Sustainable Self-Powered Sensor Systems. Adv. Funct. Mater. *31*, 2105110. https://doi.org/10.1002/adfm.202105110.

62. Dai, N., Guan, X., Lu, C., Zhang, K., Xu, S., Lei, I.M., Li, G., Zhong, Q., Fang, P., and Zhong, J. (2023). A Flexible Self-Powered Noncontact Sensor with an Ultrawide Sensing Range for Human–Machine Interactions in Harsh Environments. ACS Nano *17*, 24814–24825. https://doi.org/10.1021/acsnano.3c05507.

63. Wang, F., Ren, Z., Nie, J., Tian, J., Ding, Y., and Chen, X. (2019). Self-Powered Sensor Based on Bionic Antennae Arrays and Triboelectric Nanogenerator for Identifying Noncontact Motions. Adv. Mater. Technol. *5*, 1900789. https://doi.org/10.1002/admt.201900789.

64. Lee, J.W., Jung, S., Jo, J., Han, G.H., Lee, D.-M., Oh, J., Hwang, H.J., Choi, D., Kim, S.-W., Lee, J.H., et al. (2021). Sustainable highly charged C60-functionalized polyimide in a non-contact mode triboelectric nanogenerator. Energy Environ. Sci. *14*, 1004–1015. https://doi.org/10.1039/d0ee03057k.

65. Kim, K., Hong, J.-H., Bae, K., Lee, K., Lee, D.J., Park, J., Zhang, H., Sang, M., Ju, J.E., Cho, Y.U., et al. (2024). Extremely durable electrical impedance tomography-based soft and ultrathin wearable e-skin for

three-dimensional tactile interfaces. Sci. Adv. *10*, eadr1099. https://doi.org/10.1126/sciadv.adr1099.

66. Kim, S., Hsiao, Y.-H., Ren, Z., Huang, J., and Chen, Y. (2025). Acrobatics at the insect scale: A durable, precise, and agile micro-aerial robot. Sci. Robot. *10*, eadp4256. https://doi.org/10.1126/scirobotics.adp4256.
67. Zhao, Z., Li, W., Li, Y., Liu, T., Li, B., Wang, M., Du, K., Liu, H., Zhu, Y., Wang, Q., et al. (2025). Embedding high-resolution touch across robotic hands enables adaptive human-like grasping. Nat. Mach. Intell. *7*, 889–900. https://doi.org/10.1038/s42256-025-01053-3.
68. Xie, Y., Cheng, H., Yuan, C., Zheng, L., Peng, Z., and Meng, B. (2024). Deep learning-assisted object recognition with hybrid triboelectric-capacitive tactile sensor. Microsyst. Nanoeng. *10*, 165. https://doi.org/10.1038/s41378-024-00813-2.
69. Goh, Q.-L., Chee, P.-S., Lim, E.-H., and Ng, D.W.K. (2022). An AI-Assisted and Self-Powered Smart Robotic Gripper Based on Eco-EGaIn Nanocomposite for Pick-and-Place Operation. Nanomaterials *12*, 1317. https://doi.org/10.3390/nano12081317.
70. Shi, Q., Sun, Z., Le, X., Xie, J., and Lee, C. (2023). Soft Robotic Perception System with Ultrasonic Auto-Positioning and Multimodal Sensory Intelligence. ACS Nano *17*, 4985–4998. https://doi.org/10.1021/acsnano.2c12592.
71. Li, M., Wang, H., Fang, Z., Shi, S., Wang, Q., and Tao, A. (2024). Imaging of annulus-formation interface using reverse time migration based on ultrasonic pitch-catch measurements: Case studies from an experimental well and a field well. Ultrasonics *141*, 107323. https://doi.org/10.1016/j.ultras.2024.107323.